

PAPER

Second harmonic generation in thin permalloy film

To cite this article: P N Solovov *et al* 2021 *J. Phys. D: Appl. Phys.* **54** 425002

View the [article online](#) for updates and enhancements.

You may also like

- [Tuning the magnetic anisotropy of CoFeB grown on flexible substrates](#)
Hao Zhang, , Yuan-Yuan Li et al.
- [Magnetic heterostructures with low coercivity for high-performance magneto-optic devices](#)
V A Kotov, A F Popkov, S V Soloviev et al.
- [Time Dilation and the Length of the Second: Why Timescales Diverge](#)
Steven D. Deines and Carol A. Williams



The Electrochemical Society
Advancing solid state & electrochemical science & technology

241st ECS Meeting

May 29 – June 2, 2022 Vancouver • BC • Canada

Abstract submission deadline: Dec 3, 2021





Connect. Engage. Champion. Empower. Accelerate.
We move science forward



Submit your abstract



Second harmonic generation in thin permalloy film

P N Solovev^{1,*} , A O Afonin¹, B A Belyaev^{1,2} , N M Boev^{1,2}, I V Govorun¹, A V Izotov^{1,2} ,
A V Ugrymov¹ and A A Leksikov¹ 

¹ Kirensky Institute of Physics, Federal Research Center KSC SB RAS, 50/38 Akademgorodok, 660036 Krasnoyarsk, Russia

² Siberian Federal University, 79 Svobodny pr., 660041 Krasnoyarsk, Russia

E-mail: psolovev@iph.krasn.ru

Received 4 June 2021, revised 10 July 2021

Accepted for publication 23 July 2021

Published 3 August 2021



CrossMark

Abstract

Second harmonic generation versus strength and direction of the applied static magnetic field was measured for a thin permalloy ($\text{Ni}_{80}\text{Fe}_{20}$) film in a microstrip line at a driving frequency of 1 GHz and maximum input power of ~ 110 mW. The measurements revealed two peaks in the double frequency signal—in the low static field (~ 10 Oe) and the high one (~ 45 Oe). To explain these findings, a macrospin model of a thin magnetic film with in-plane uniaxial magnetic anisotropy was considered. A perturbation expansion of the Landau–Lifshitz–Gilbert equation provided an explanation of the experimental data. The analysis of the model revealed that the low-field peak was caused by the longitudinal second-order magnetization component and the high-field peak by the transversal one. It was also shown that the uniaxial magnetic anisotropy of the film and the dependence of the magnetic damping parameter on the applied field play an important role in the process of the second harmonic generation. The results obtained give insights into some peculiarities of the nonlinear magnetization dynamics that are important in the development of magnetic film-based devices in the field of microwave signal processing and manipulation.

Keywords: ferromagnetic resonance, frequency doubling, nonlinear dynamics, thin magnetic film, second harmonic

(Some figures may appear in colour only in the online journal)

1. Introduction

Nonlinear dynamics in magnetic materials is a topic of intensive experimental and theoretical research due to its great importance from both the fundamental and application viewpoints [1–4]. There are a large variety of nonlinear effects that emerge at high input powers, including instability processes associated with the parametric excitation of spin waves [5–7], foldover effects [8], auto-oscillations [9], and others [10–12]. However, even in the case of the relatively low amplitude of rf driving field, the magnetization precession nevertheless

demonstrates some nonlinear responses, the most prominent of which is the emergence of the magnetization components that oscillate at double the frequency of the driving field. This phenomenon was extensively investigated in ferrites since the late 1950s [13–17]. It was first found that in the standard configuration, when the driving field was perpendicular to the static magnetic field, the second harmonic signal was caused by the longitudinal (i.e. along the equilibrium magnetization) component of the dynamic magnetization, with generation efficiency determined by the ellipticity of the precession orbit [18]. Later it was also shown that another, transverse double frequency component could be excited by an ‘oblique’ driving field, which longitudinal component made a modulating contribution [19, 20].

* Author to whom any correspondence should be addressed.

In recent years, the focus of studies has shifted from ferrites towards thin metallic magnetic films and nanostructures, owing to their ability to be readily incorporated in on-wafer devices, with an additional opportunity to control their functionality using spin transport. Studies on the nonlinear behavior of permalloy films using coplanar or microstrip waveguides have demonstrated the possibility of input signal frequency multiplying [21], mixing [22, 23], and parametric amplification [24]. Moreover, more recently it has been shown that second-order nonlinear effects play a vital role in spin wave propagation properties of thin film-based micron-sized structures [25–28]. Specifically, experiments revealed that spin wave propagated in permalloy microstrips efficiently generated another wave at the double frequency [25, 26]. It was suggested and later confirmed with micromagnetic simulations [28] that this second wave originated from the dynamic demagnetizing field generated at the stripe edges by the second-order longitudinal magnetization component. This emphasizes the importance of a detailed understanding of the nonlinear processes in thin magnetic films and, particularly, the second-order effects.

In this paper, we experimentally and theoretically investigate the processes of the second harmonic generation in a thin permalloy film placed inside a microstrip transmission line. The focus of the paper is on how the generation efficiency depends on the applied static magnetic field. For this, we measure the power of double frequency signal as a function of the strength and direction of the static field and compare the experimental data with the results of the Landau–Lifshitz–Gilbert equation solution obtained using a perturbation theory in a macrospin approximation.

2. Experimental details

2.1. Sample preparation

For all measurements of the second harmonic generation presented below, we used the same permalloy (NiFe) thin-film sample. The film was produced by dc magnetron sputtering from Ni₈₀Fe₂₀ wt% target at a base pressure of 2.2×10^{-6} Torr and argon pressure of 1.5×10^{-3} Torr. The film was deposited on a heated quartz glass $5 \times 3 \times 0.5$ mm³ size substrate preliminary covered by SiO layer 500 nm in thickness to improve the homogeneity of the film. During the deposition, a static magnetic field of about 200 Oe was applied in the film plane to induce the uniaxial magnetic anisotropy with the easy axis (EA) of magnetization oriented along the long side of the sample. The thickness of the film was about 100 nm (measurement error is 5%), and its composition was close to the nominal composition of the target (the difference is less than 1 wt%), which was confirmed by an x-ray fluorescence analysis.

2.2. Sample characterization

The basic film magnetic properties were determined by local ferromagnetic resonance (FMR) measurements. For this, we used the scanning FMR spectrometer based on a microstrip

resonator with a hole in the ground plane [29, 30]. The spectrometer allows for measurements of the resonance field angular dependencies at a fixed pumping frequency from local areas (about 0.8 mm²) of the film surface with very high accuracy. From these data, using a special fitting procedure [31], we extracted effective saturation magnetization and uniaxial anisotropy parameters. To study the properties of the sample in a wide frequency range, we used a shorted microstrip line technique [32]. The Vector Network Analyzer (VNA, R&S ZNB) was used to measure the reflected power (S_{11} parameter) of a signal that was fed to a shorted microstrip line with the investigated sample inside. The measurements were done in the frequency sweep mode for a set of in-plane static magnetic field values. To increase the signal-to-noise ratio, we applied the usual procedure of subtracting the background signal from the total one to isolate the part associated with the absorption by the magnetic film [33].

2.3. Measurement setup

The investigation of second harmonic generation in the thin magnetic film was performed on a specially designed setup. A scheme of the measurement configuration is shown in figure 1. A pair of calibrated Helmholtz coils was used to apply an in-plane static magnetic field of up to 100 Oe to the sample. A dc power was supplied to the coils through a computer-controlled dc source. The coils were mounted on a platform rotated (0° – 180°) by a stepper motor.

The microwave signal was transmitted to and received from the sample through a microstrip line. The sample was inserted into the transmission line between the signal line and ground plane, with magnetic film facing the signal line of width $w = 1$ mm. The microstrip line was designed to have characteristic impedance $Z_0 = 50 \Omega$. The rf signal at the frequency of 1 GHz from the microwave generator passed through a bandpass filter BPF1 having a passband at the frequency of 1 GHz. This filter helped to purify the input signal by filtering out harmonic and non-harmonic components of the signal at the output of a microwave generator. The second bandpass filter, BPF2, with passband at the frequency of 2 GHz, was placed at the output of the transmission line. It protected the input circuit of a spectrum analyzer from the 1 GHz signal. It also almost doubled the magnitude of the rf magnetic field by reflecting the input signal back to the transmission line. The isolator was used to protect the generator from this reflected signal. After filtering by BPF2, the rf signal consisting only of the second-harmonic component reached the spectrum analyzer for measurements of its power. The filters used were of our design and fabrication [34].

All components of the setup (dc and rf sources, spectrum analyzer, stepper motor) were controlled by a computer with our developed MATLAB-based software, allowing us to automate the measurement process. In particular, this made it possible to measure the dependencies of second-harmonic generation on the direction and strength of the static magnetic field with high accuracy. We note that we chose the frequency of the input signal to be 1 GHz because, for this frequency, the FMR field is yet large enough to saturate a thin-film permalloy

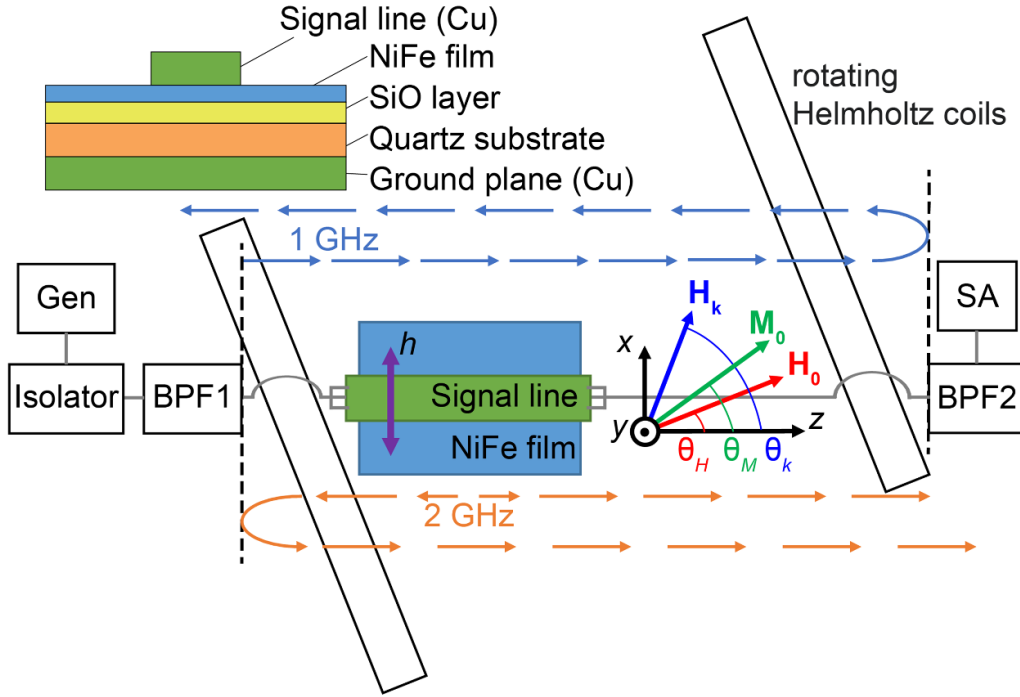


Figure 1. Experimental setup for the second harmonic measurements and the coordinate system. Gen: microwave generator R&S SMA100B; BPF1 and BPF2: bandpass filters at 1 and 2 GHz; SA: spectrum analyzer R&S FSW. Blue and orange arrows schematically show the signals propagating at frequencies of 1 and 2 GHz. Schematic side view of the sample is shown in the upper left corner.

sample. At the same time, the magnetic susceptibility is still high, allowing for the accurate detection of second-order non-linear effects without the need for increasing the input power.

3. Theoretical model of a thin magnetic film

For a theoretical analysis of the experimental data, we will use a macrospin model of a thin magnetic film and calculate its magnetization dynamics using a perturbation theory [35, 36]. The free energy density of a thin magnetic film with an in-plane uniaxial anisotropy in an external magnetic field \mathbf{H} can be expressed as

$$F = -\mathbf{M}\mathbf{H} + \frac{1}{2}\mathbf{M}N^{\text{eff}}\mathbf{M}, \quad (1)$$

where $N^{\text{eff}} = N + N_k$ is an effective demagnetizing tensor. Here, N is a tensor that is associated with the shape of a sample, and N_k is a tensor that describes the uniaxial magnetic anisotropy. For the geometry in figures 1 and 2, N has only one nonzero component $N_{yy} = 4\pi$, while tensor N_k is determined as

$$N_k = -\frac{H_k}{M} \begin{pmatrix} n_x^2 & 0 & n_x n_z \\ 0 & 0 & 0 \\ n_x n_z & 0 & n_z^2 \end{pmatrix}, \quad (2)$$

where n_x, n_y, n_z are the components of a unit vector \mathbf{n} that coincides with the EA of magnetization, and M is the length of the magnetization vector \mathbf{M} .

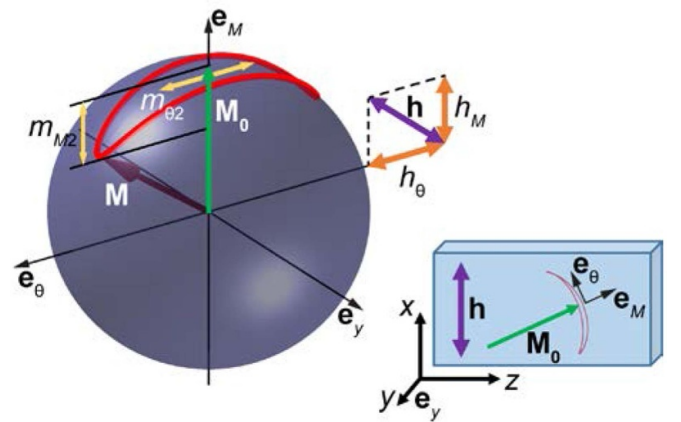


Figure 2. The nonlinear dynamics of magnetization in a thin magnetic film.

The dynamics of the magnetization \mathbf{M} is described by the Landau–Lifshitz–Gilbert equation

$$\frac{\partial \mathbf{M}}{\partial t} = -\gamma \mathbf{M} \times \mathbf{H}^{\text{eff}} + \frac{\alpha}{M} \mathbf{M} \times \frac{\partial \mathbf{M}}{\partial t}, \quad (3)$$

where the effective magnetic field acting on the magnetization is determined as $\mathbf{H}^{\text{eff}} = -\partial F / \partial \mathbf{M} = \mathbf{H} - N^{\text{eff}}\mathbf{M}$.

The differential equation (3) is nonlinear. To find its approximate solution, we use the perturbation theory. Let us expand the magnetization to up to a second-order term to obtain the expressions for calculation of magnetization components oscillating at a double frequency of the

driving field. By considering both the magnetization and effective magnetic field as the sum of static and dynamic parts, the solution of equation (3) will be sought in the form $\mathbf{M} = \mathbf{M}_0 + \mathbf{m}_1(t) + \mathbf{m}_2(t)$, $\mathbf{H} = \mathbf{H}_0 + \mathbf{h}(t)$, in the limits $m_2 \ll m_1 \ll M_0$, and $h \ll H_0$. We note that in this approximation it is also assumed that the length

of the time-independent (equilibrium) magnetization \mathbf{M}_0 is equal to the saturation magnetization M_s of the sample, i.e. $|\mathbf{M}_0| = |\mathbf{M}| = M_s$.

In the coordinate system that is related to the equilibrium magnetization \mathbf{M}_0 , (\mathbf{e}_θ , \mathbf{e}_y , \mathbf{e}_M) (figure 2), the N^{eff} tensor is transformed to

$$N^{\text{eff}} = -\frac{1}{M_s} \begin{pmatrix} H_k \sin^2(\theta_k - \theta_M) & 0 & H_k \sin 2(\theta_k - \theta_M)/2 \\ 0 & -4\pi M_s & 0 \\ H_k \sin 2(\theta_k - \theta_M)/2 & 0 & H_k \cos^2(\theta_k - \theta_M) \end{pmatrix}, \quad (4)$$

where θ_k is the angle of EA orientation, and θ_M is the angle of the equilibrium magnetization \mathbf{M}_0 . The effective magnetic field is given by

$$\begin{aligned} \mathbf{H}^{\text{eff}} &= \mathbf{H}_0^{\text{eff}} + \mathbf{h}^{\text{eff}} \\ \mathbf{H}_0^{\text{eff}} &= \mathbf{H}_0 - N^{\text{eff}} \mathbf{M}_0 \\ \mathbf{h}^{\text{eff}} &= \mathbf{h} - N^{\text{eff}} \mathbf{m}_1 - N^{\text{eff}} \mathbf{m}_2, \end{aligned} \quad (5)$$

and equation of motion (3) is

$$\begin{aligned} \frac{\partial(\mathbf{m}_1 + \mathbf{m}_2)}{\partial t} + \frac{\alpha}{M_s} \frac{\partial(\mathbf{m}_1 + \mathbf{m}_2)}{\partial t} \times (\mathbf{M}_0 + \mathbf{m}_1 + \mathbf{m}_2) \\ = \gamma(\mathbf{H}_0^{\text{eff}} + \mathbf{h}^{\text{eff}}) \times (\mathbf{M}_0 + \mathbf{m}_1 + \mathbf{m}_2). \end{aligned} \quad (6)$$

In the zero-order approximation, by neglecting dynamic components $\mathbf{m}_1(t)$, $\mathbf{m}_2(t)$, and $\mathbf{h}(t)$, we get the condition for the determination of equilibrium magnetization

$$\mathbf{M}_0 \times \mathbf{H}_0^{\text{eff}} = 0. \quad (7)$$

In the first-order approximation, retaining the first-order terms $\mathbf{m}_1(t)$ and $\mathbf{h}(t)$, we obtain the linearized equation

$$\begin{aligned} \frac{\partial \mathbf{m}_1}{\partial t} + \frac{\alpha}{M_s} \frac{\partial \mathbf{m}_1}{\partial t} \times \mathbf{M}_0 + \gamma(N^{\text{eff}} \mathbf{m}_1) \times \mathbf{M}_0 + \gamma \mathbf{m}_1 \\ \times \mathbf{H}_0^{\text{eff}} = \gamma M_s \mathbf{G}, \end{aligned} \quad (8)$$

where $\mathbf{G} = (1/M_s)[\mathbf{h} \times \mathbf{M}_0]$ is an effective vector of linear excitation.

In the second-order approximation, taking into account equations (7) and (8), we obtain the equation for calculation of the second-order dynamic magnetization $\mathbf{m}_2(t)$

$$\begin{aligned} \frac{\partial \mathbf{m}_2}{\partial t} + \frac{\alpha}{M_s} \frac{\partial \mathbf{m}_2}{\partial t} \times \mathbf{M}_0 + \gamma(N^{\text{eff}} \mathbf{m}_2) \times \mathbf{M}_0 + \gamma \mathbf{m}_2 \\ \times \mathbf{H}_0^{\text{eff}} = \gamma M_s \mathbf{F}, \end{aligned} \quad (9)$$

where $\mathbf{F} = (1/M_s)\{\mathbf{h} \times \mathbf{m}_1 + \mathbf{m}_1 \times (N^{\text{eff}} \mathbf{m}_1)\}$ is an effective vector of nonlinear excitation. It is important to note that the differential equations (8) and (9) are of the same form, thus for

the solution of equation (9) we can use the results of solution of equation (8) with the substitution of vector \mathbf{G} by the corresponding components of vector \mathbf{F} .

In the [appendix](#), we provide the derivation of the full expressions for the first- and second-order magnetization components (complex amplitudes), which are quite lengthy. However, their analysis shows that only a small number of terms give the most significant contribution, while others can be safely neglected as their values at least one order of magnitude smaller. This is because of the shape anisotropy of the thin-film sample, which results in almost zero out-of-plane components of magnetization.

4. Results and discussion

4.1. Magnetic characteristics of the sample

From the measurements with the scanning FMR spectrometer at a fixed pumping frequency of 2.5 GHz, we determined the following magnetic characteristics of the investigated sample: the effective saturation magnetization $M_s = 872 \pm 3$ emu cm⁻³, the uniaxial anisotropy field $H_k = 3 \pm 0.6$ Oe, the angle of EA orientation (figure 1) $\theta_k = -0.5 \pm 1.5^\circ$, and the full width at half maximum field-sweep FMR linewidth $\Delta H = 17 \pm 0.74$ Oe. These values were obtained by averaging locally measured parameters over the whole film surface, while the values with the ‘plus-minus’ sign next to them show the standard deviation of the parameter. The results indicate that the film is quite homogeneous. The largest deviations from the mean values were observed at the edges of the sample; these effects were investigated in detail in our previous paper [37].

Using the VNA-FMR setup, we measured the absorption spectra of the sample in a broad range of fields ($H_0 = 0$ –120 Oe) and frequencies ($f = 0.1$ –4 GHz) when the in-plane static magnetic field H_0 was applied along the EA of the film (figure 3). The map shows a usual $f_{\text{FMR}}(H_0)$ dependence of the FMR without any additional oscillation modes. From these spectra, we extracted the dependence of the field-swept linewidth ΔH on the driving frequency (figure 4(a)).

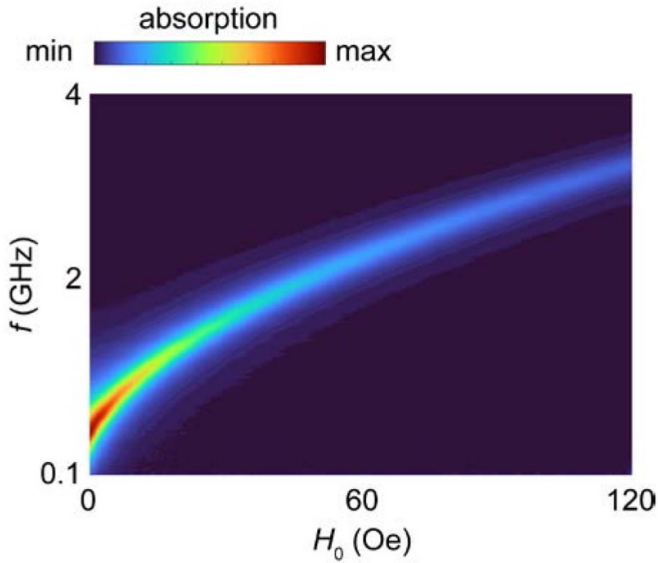


Figure 3. Absorption spectra map obtained with VNA-FMR showing field dependence of the FMR frequency.

As follows from the classical theory of FMR [35], the linewidth should linearly depend on the frequency

$$\Delta H = 4\pi f_{\text{FMR}} \alpha / \gamma, \quad (10)$$

where α is the damping parameter, $\gamma = 1.76 \times 10^7 \text{ rad s}^{-1}$, Oe is the gyromagnetic ratio, and f_{FMR} is the FMR frequency. In figure 4(a), the red line shows the dependence (10) fitted to the experimental data for $f > 1 \text{ GHz}$, with $\alpha = 0.009$. However, at lower frequencies, the experimental data for $\Delta H(f)$ deviates from the linear dependence and tends to a value of about 5.5 Oe at $f \approx 0$. It has been suggested that this behavior is caused by magnetic inhomogeneities in the film [38], and particularly by magnetization ripple observed in nanocrystalline samples [39–42]. By using experimental dependencies $\Delta H(f)$, $f_{\text{FMR}}(H_0)$, and equation (10), we can obtain the dependence of the (effective) damping parameter α on the applied field H_0 (figure 4(b)). Here, the red line corresponds to the value of α calculated from the linear fit. Figure 4(b) demonstrates that in the low-field (LF) region, α can be 1.5 times higher than its base (high-field) value. This is an important fact that we will use in an analysis of the second-harmonic generation in later sections of this paper.

4.2. Second harmonic generation measurements

Figure 5(a) demonstrates the map of the second harmonic generation. These data were obtained by measuring the output power P_2 at $f_2 = 2 \text{ GHz}$ by the spectrum analyzer while rotating the Helmholtz coils in the range of angles θ_H from 0° to 180° with 2° step and varying the static field strength H_0 from 1 to 60 Oe with 1 Oe step (0.5 Oe near peaks). The power of the input signal at $f_1 = 1 \text{ GHz}$ was $P_1 = 54 \text{ mW}$. The observed mirror symmetry in the angular dependence with the symmetry axis at $\theta_H = 90^\circ$ is due to the geometry of the measurement configuration (figure 1). Figure 5(a) indicates that along

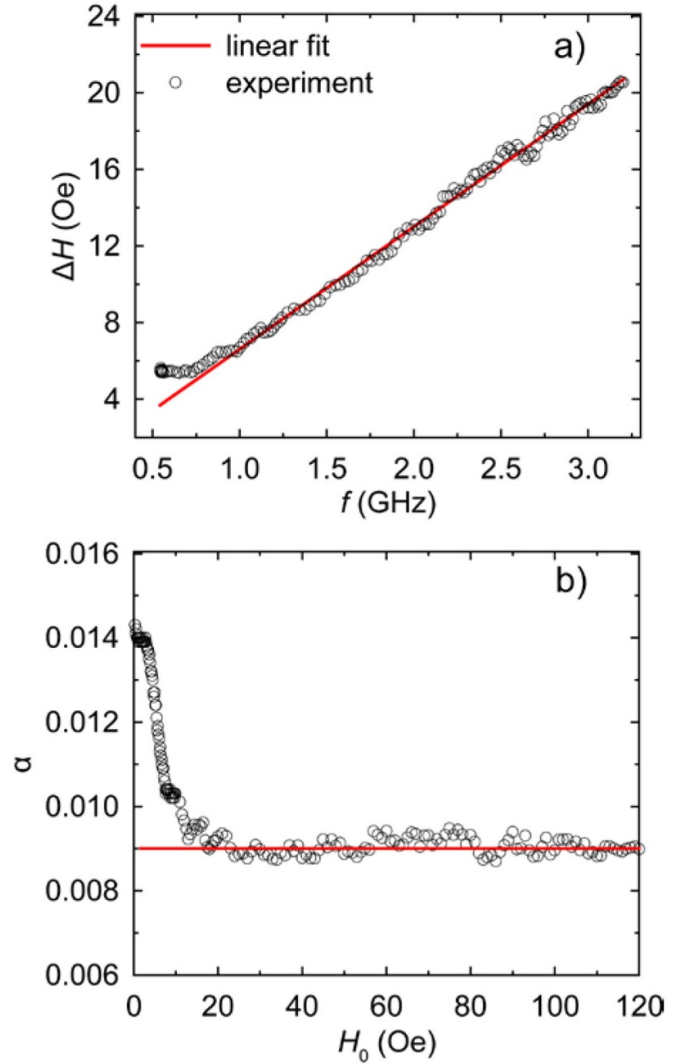


Figure 4. (a) FMR linewidth ΔH versus pumping frequency f . (b) The dependence of the damping parameter α on the applied field H_0 , extracted from (a).

the field axis, there are two peaks of second harmonic generation: the first one is observed at $H_0 = 9.5 \text{ Oe}$ and $\theta_H = 48^\circ$, which will be denoted as the LF peak, and the second one is at $H_0 = 45.5 \text{ Oe}$ and $\theta_H = 42^\circ$ (the high-field (HF) peak). Figure 5(b) shows the dependence $P_2(H_0)$ obtained using the same data as in figure 5(a). This is a cross-section of the map in figure 5(a) where each P_2 value was picked for an optimal angle θ_H at which for a given value of H_0 the power P_2 is maximum. Although the HF peak is much lower than the LF (the LF/HF power ratio is 106) and on a linear scale the HF peak vanishes (see inset in figure 5(b)), it is clearly distinguished on a logarithmic scale. Comparing the parameters of the LF peak and the $f_{\text{FMR}}(H_0)$ dependence in figure 3, it is apparent that this maximum of the second harmonic generation is associated with the FMR. However, the linear model of FMR does not show any peculiarities at higher than FMR fields, where the HF peak is observed.

We also measured the second harmonic power at LF and HF peaks by varying the input power in a range of 0.02–108 mW.

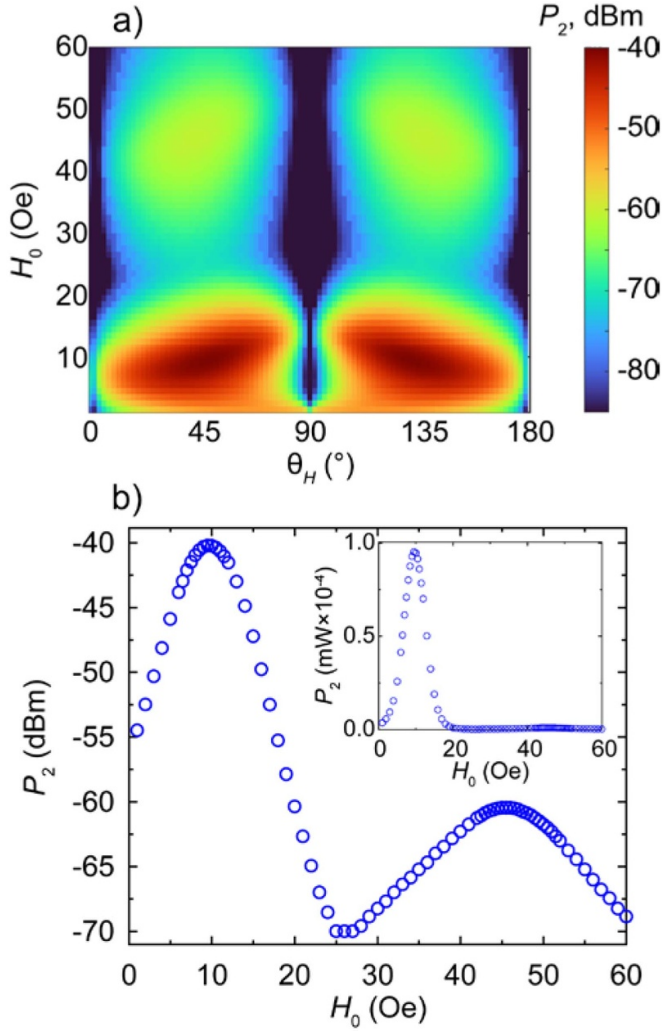


Figure 5. (a) Map of the second harmonic generation showing the power P_2 at a double frequency $f_2 = 2$ GHz (in log scale) as a function of the direction θ_H and strength H_0 of the static magnetic field. The input power at $f_1 = 1$ GHz was $P_1 = 54$ mW. (b) The $P_2(H_0)$ dependence, plotted using the same data as in (a) for optimal values of θ_H at which for a given value of H_0 the power P_2 is maximum. The inset shows the same dependence on a linear scale.

These data are plotted in figure 6 but for the values $P_2^{1/2}(P_1^{1/2})$, because amplitudes of rf magnetic field and magnetization are proportional to the square root of the power (this will be discussed in more detail later in this paper). The experimental data indicate a quadratic dependence of the second harmonic generation on the input rf power for both peaks. However, a closer look reveals that the LF peak starts to deviate from the quadratic dependence near the end of the input power range. We believe that this is caused by the onset of Suhl spin wave instability processes [7]. At the same time, no deviation is observed for the HF peak. This might be related to the fact that to instability processes occur, the conditions of spin wave existence determined by the dispersion relation must be met. This is the case for the LF peak, but for the HF peak there are no available spin wave modes in this frequency-field region.

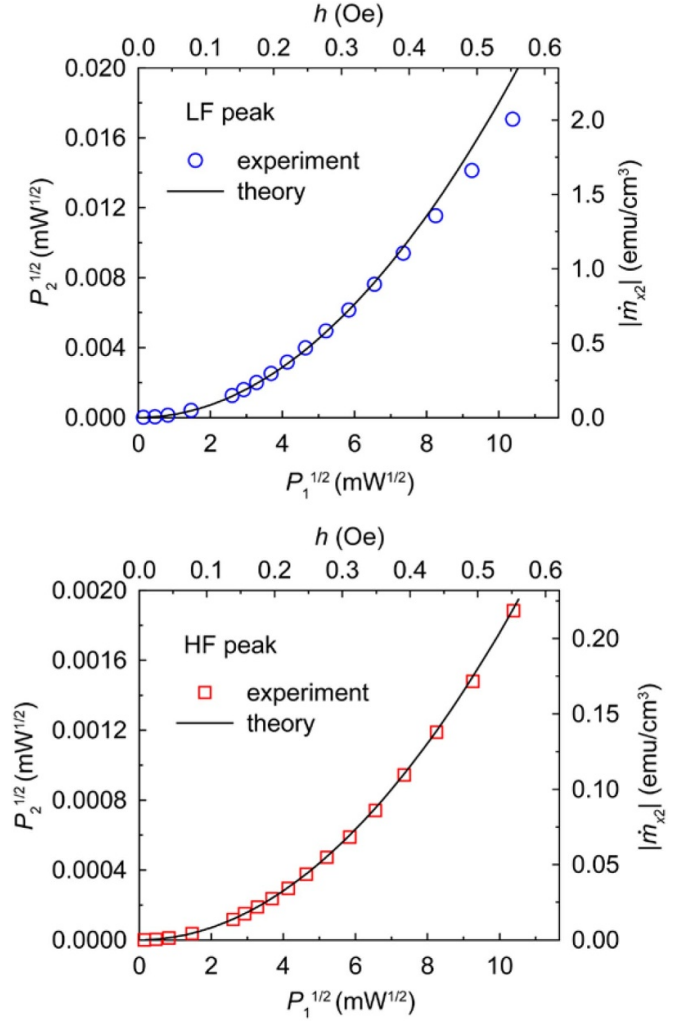


Figure 6. The dependencies of the second harmonic generation on the input signal for the LF and HF peaks. Left and bottom axes are the square roots of the input P_1 and output P_2 powers; right and top axes are amplitudes of rf magnetic field and magnetization.

4.3. Theoretical analysis of second-order magnetization components

To explain the experimentally observed dependencies of the second harmonic generation, we will use a macrospin model of a thin magnetic film, which was described in section 3. An intuitive picture of the origin of a double frequency magnetization component is presented in figure 2. Excited by a linearly polarized microwave magnetic field \mathbf{h} , the magnetization vector \mathbf{M} will process in an elliptical orbit in the $(\mathbf{e}_\theta, \mathbf{e}_y)$ plane. In the case of a thin magnetic film, this ellipticity is greatly enhanced due to large demagnetizing factors preventing magnetization escape from the film plane. Since the length of the magnetization vector \mathbf{M} must not change, a longitudinal component m_{M2} appears, which oscillates in time at a double frequency of the driving field. As we will show below, another component, $m_{\theta 2}$, can contribute to the resulting second harmonic signal.

The main component of the first-order magnetization can be expressed as $\dot{m}_{\theta 1} = \chi_\theta h_\theta$, where χ_θ is θ -component of

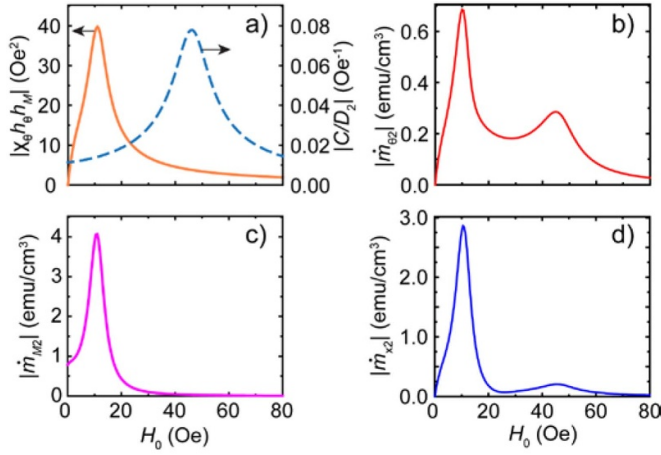


Figure 7. The amplitudes of second-order magnetization components versus static field H_0 , calculated for a driving field frequency of 1 GHz and amplitude of 0.55 Oe.

the magnetic susceptibility tensor, and the overdot denotes that $\dot{m}_{\theta 1}$ is the complex amplitude (see the appendix, equation (A6)). The first-order magnetization has the frequency of the driving field ω_1 . It depends linearly on the driving field and has maximum amplitude in the conditions of the FMR and when \mathbf{h} is perpendicular to the equilibrium magnetization \mathbf{M}_0 .

The second-order magnetization has the double frequency of the driving field, $\omega_2 = 2\omega_1$. The main contributing components of the second-order magnetization are \dot{m}_{M2} and $\dot{m}_{\theta 2}$. The amplitude of the longitudinal component \dot{m}_{M2} can be approximately expressed as $|\dot{m}_{M2}| \approx (1/4M_s) |\dot{m}_{\theta 1}^2| = (1/4M_s) |\chi_\theta^2 h_\theta^2|$ (see equation (A11)). It gives the largest contribution to \mathbf{m}_2 and reaches a maximum at the same conditions as $\dot{m}_{\theta 1}$. This is illustrated in figure 7, where we plotted the dependencies of the second-order magnetization components amplitudes on the applied field H_0 at a fixed driving frequency $f_1 = \omega_1/2\pi = 1$ GHz. Material parameters M_s and H_k corresponded to the experimentally determined values 872 emu cm^{-3} and 3 Oe , the damping parameter $\alpha = 0.009$ was constant, $\theta_k = 0^\circ$, $\theta_H = 45^\circ$, and $h = 0.55 \text{ Oe}$. The maximum of $|\dot{m}_{M2}|$ (figure 7(c)) corresponds to the LF peak observed in the experiment.

The behavior of the transverse component $\dot{m}_{\theta 2}$ is a bit more complicated. After some simplifications, we can write the amplitude of $\dot{m}_{\theta 2}$ as $|\dot{m}_{\theta 2}| \approx |(1/D_2)C\chi_\theta h_\theta h_M|$, where the coefficient C can be approximated as a constant (see equation (A11)), and D_2 depends on H_0 and ω_2 (see equation (A4)). As shown in figure 7(a), the part $|\chi_\theta h_\theta h_M|$ of $|\dot{m}_{\theta 2}|$ has maximum in the FMR, as all the components analyzed before. However, $|1/D_2|$ reaches a maximum at half the frequency of FMR, or in the case of fixed frequency, for the corresponding to that condition applied field H_0 . As a result, $|\dot{m}_{\theta 2}|$ exhibits two peaks on the H_0 dependence (figure 7(b)). While the first peak coincides with $|\dot{m}_{M2}|$ maximum and does not contribute much to the resulting output signal, it is the second peak that of most interest because it explains the experimentally observed HF peak. The projection of \mathbf{m}_2 on

the ‘sensitive’ direction (the x -axis) of the microstrip line, which produces the resulting second-harmonic output signal, is determined as

$$|\dot{m}_{x2}| = |\dot{m}_{\theta 2}| \cos \theta_M + |\dot{m}_{M2}| \sin \theta_M. \quad (11)$$

Its dependence on the applied field H_0 is shown in figure 7(d).

We should also note that the second-order components depend quadratically on the driving field amplitude. However, while \dot{m}_{M2} depends only on a transverse field h_θ , $\dot{m}_{\theta 2}$ is a function of product of transverse h_θ and longitudinal h_M components meaning that $\dot{m}_{\theta 2}$ can be excited only by an ‘oblique’ microwave field.

4.4. Comparison to experiment

To compare the theory and experiment, it is necessary to express the amplitudes of the microwave field h and magnetization component $|\dot{m}_{x2}|$ as functions of the input and output powers. An rf magnetic field produced by a microstrip line of width w can be approximately expressed as

$$h = d_h \sqrt{\frac{P_1}{4Z_0 w^2}}, \quad (12)$$

where d_h is an ‘amplification’ coefficient arising due to the reflection of the input signal from the BPF2 filter (figure 1). From additional measurements, we estimated the coefficient d_h to be 1.9.

The magnetic flux produced by the magnetization \mathbf{m}_2 that winds around the signal line in the SI system of units can be written as [43] $\Phi = 0.5d_m\mu_0\mathbf{m}_2(t)lt_F$, where l and t_F are the length and thickness of a magnetic film, and μ_0 is the magnetic constant. The d_m coefficient accounts for losses of various types, including non-zero spacing, skin effect, etc. In this paper, we consider this coefficient as a fitting parameter. The time-averaged power could be calculated as $\langle P \rangle = \frac{1}{T} \int_0^T P(t) dt = \frac{1}{T} \int_0^T \frac{U(t)^2}{Z_0} dt$, where $U(t) = -d\Phi/dt$ is the voltage induced in the microstrip line, and $T = 2\pi/\omega_2$. Thus, we have

$$\langle P \rangle = \frac{(0.5\mu_0 d_m l t_F)^2 \omega_2}{Z_0} \frac{1}{2\pi} \int_0^{2\pi/\omega_2} \left(\frac{d\mathbf{m}_2}{dt} \right)^2 dt. \quad (13)$$

Since $\mathbf{m}_2(t) = (\dot{\mathbf{m}}_2 \cdot e^{i\omega_2 t} + \dot{\mathbf{m}}_2^* \cdot e^{-i\omega_2 t})/2$, the integral with \mathbf{m}_2 in equation (13) is simply $\pi\omega_2 |\dot{\mathbf{m}}_2|^2$. Therefore, the amplitude of the second-order component $|\dot{m}_{x2}|$ can be estimated from the output power P_2 as

$$|\dot{m}_{x2}| = \frac{2\sqrt{2P_2 Z_0}}{d_m \omega_2 \mu_0 l t_F}. \quad (14)$$

Note that expressions (12) and (14) were obtained in the SI system of units. To convert to the cgs units used in this paper, the h value from equation (12) should be multiplied by $4\pi/10^3$, and $|\dot{m}_{x2}|$ of equation (14) by 10^{-3} .

We then calculated the theoretical dependencies of $|\dot{m}_{x2}|$ (using equation (11)) on the direction and strength of the applied static field and the amplitude of the microwave driving field. As in the previous section, we used the parameters $M_s = 872 \text{ emu cm}^{-3}$, $H_k = 3 \text{ Oe}$, $\theta_k = 0^\circ$, and the driving frequency $f_1 = \omega_1/2\pi = 1 \text{ GHz}$. However, here we also considered the field dependence of the damping parameter $\alpha(H_0)$ determined experimentally (figure 4(b)). The amplitude of the driving field h used in the calculations was determined from equation (12), where the experimental input powers were substituted. The experimental values of the second-order magnetization $|\dot{m}_{x2}|$ were calculated from equation (14). By fitting the experimental dependencies of $|\dot{m}_{x2}|(h)$ simultaneously for the LF and HF peaks to the theoretical ones (figure 6), we determined that the loss parameter d_m of equation (14) had a reasonable value of 0.62.

Now, finally, we can compare the theoretical and experimental maps of $|\dot{m}_{x2}|(\theta_H, H_0)$. They are presented in figure 8. The experimental one was obtained from the data in figure 5(a) using equation (14). The theoretical map was calculated for $h = 0.4 \text{ Oe}$ determined from equation (12), with $P_1 = 54 \text{ mW}$. The plots demonstrate almost perfect agreement. The theory reproduces all the features of the experiment, including the positions of the LF and HF peaks, their linewidths, and magnitudes. This is clearly seen in figure 9(a), where the dependencies of the second-order magnetization $|\dot{m}_{x2}|$ on the static field H_0 are shown, with circle symbols corresponding to the experiment and lines to the theory. Similar to figure 5(b), these dependencies are the cross-sections of the maps in figure 8 (shown there with white lines), where each $|\dot{m}_{x2}|$ value was picked for an optimal angle θ_H^{opt} at which for a given value of H_0 , the amplitude $|\dot{m}_{x2}|$ is maximum.

In figure 9(a), we plotted the theoretical dependencies obtained for the field-depended damping parameter $\alpha(H_0)$ (solid line) and the constant $\alpha = 0.009$ (dashed line). One can see that the consideration of $\alpha(H_0)$ is necessary to reproduce the experiment accurately in the LF region due to the additional contribution to the FMR linewidth associated with magnetic inhomogeneities in the sample. The use of constant α leads to the overestimation of the $|\dot{m}_{x2}|$ LF peak of 27%. However, even with this correction, there is still a discrepancy between the positions of the calculated and experimental LF peaks, about 1 Oe. Although this discrepancy is small, it is larger than the measurement error that we estimate to be 0.5 Oe or so. The origin of the divergence might be related to the higher-order components of magnetization that we did not account for in calculations. As figure 9(a) indicates, by accounting for both components \dot{m}_{M2} and $\dot{m}_{\theta2}$, the uniaxial anisotropy, and field dependence of the damping parameter, we have achieved a remarkable agreement of the theoretically calculated second-order magnetization $|\dot{m}_{x2}|$ with the experimental one, including the ratio of LF to HF peak (experiment 10.3, theory 10.5), without the need of including some additional mechanisms of absorption, as it was done, for example, in [21].

Figure 9(b) demonstrates the optimal angle θ_H^{opt} at which $|\dot{m}_{x2}|$ is maximum as a function of the static field H_0 . There is

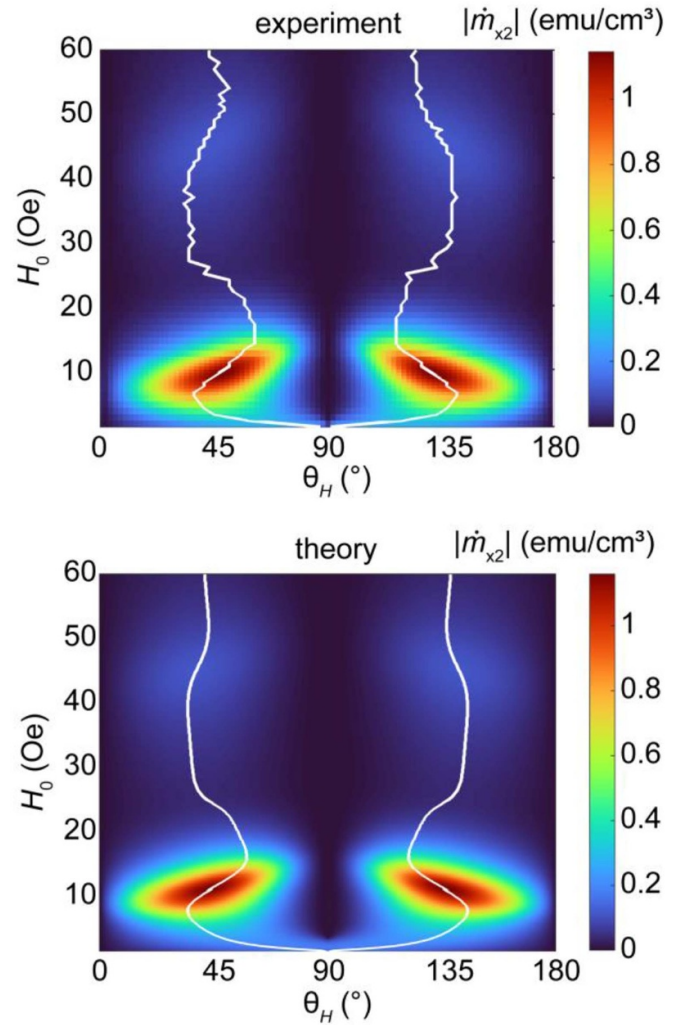


Figure 8. The experimental and theoretical maps showing the amplitude of the second-order magnetization $|\dot{m}_{x2}|$ as a function of the direction θ_H and strength H_0 of the static magnetic field. The input power at $f_1 = 1 \text{ GHz}$ was 54 mW that corresponded to the rf magnetic field of 0.4 Oe. White lines show $|\dot{m}_{x2}|$ for optimal angles of field direction θ_H^{opt} at which for a given value of H_0 , $|\dot{m}_{x2}|$ is maximum.

also a fairly good agreement between theory and experiment, although one can see that the theoretical curve is shifted from the experimental one to the lower angles by about 5° ; the origin of this shift is unclear.

The behavior of the optimum angle $\theta_H^{\text{opt}}(H_0)$ can be explained by considering two main contributing mechanisms. The first one arises from the geometry of the measurement setup, as the microstrip line is the source of the driving rf field, and at the same time, the detector of the magnetic flux. For the LF peak, as follows from equation (11), we can write $|\dot{m}_{x2}| \approx |\dot{m}_{M2}| \sin \theta_M \sim |\chi_\theta^2 h_\theta^2| \sin \theta_M$, with $h_\theta = h \cos \theta_M$. Thus, we obtain the condition for the determination of the ‘geometrical’ optimal orientation of the equilibrium magnetization $\partial(\cos^2 \theta_M \sin \theta_M) / \partial \theta_M = 0$, which gives $\theta_M = 35.3^\circ$. Because of the uniaxial anisotropy, θ_M does not equal θ_H but approaches it with the increase of the field strength. Apart from

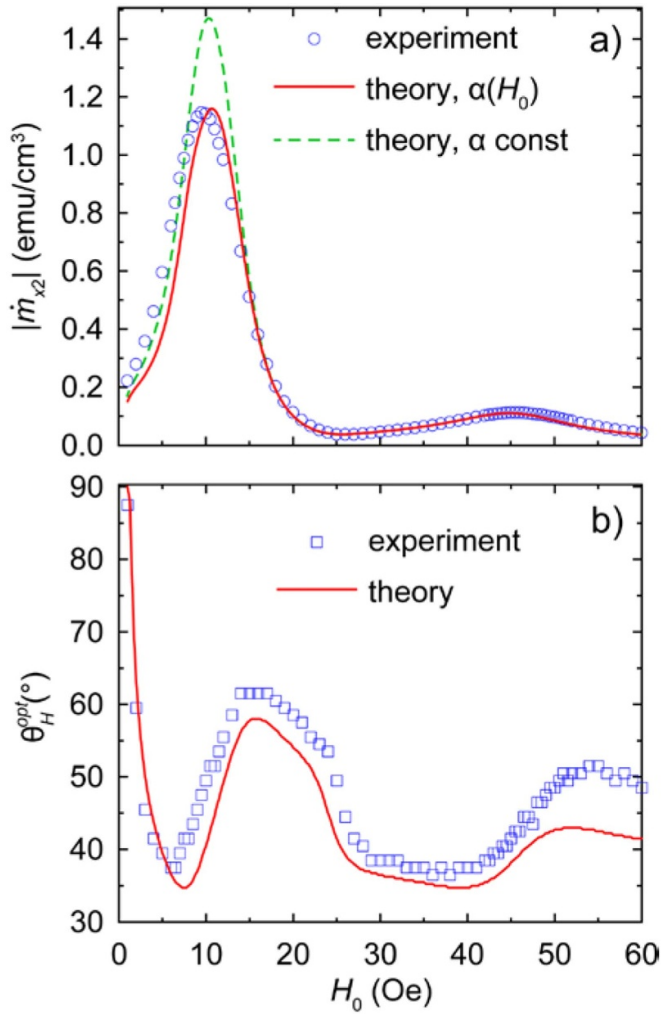


Figure 9. (a) The amplitude of the second-order magnetization $|m_{x2}|$ versus static field H_0 , for optimal angles of field direction θ_H^{opt} at which for a given value of H_0 , $|m_{x2}|$ is maximum. (b) Optimal angle θ_H^{opt} versus static field H_0 .

the geometry, another impact to the optimal angle dependence $\theta_H^{opt}(H_0)$ is from the magnetic susceptibility χ with the maximum in the FMR. For a given value of the static field H_0 the FMR occurs at a specific angle θ_H and corresponding θ_M , which is not necessarily equal to the geometrical optimal value 35.3° . Therefore, the optimal angle of the second harmonic generation θ_H^{opt} is determined by the balance between the geometry and the FMR conditions. This is illustrated in figure 10, where we plot the dependence of the susceptibility tensor component $|\chi_\theta|$ on the static field direction θ_H and strength H_0 . On top of this map, the black solid line shows the calculated optimal angle of the equilibrium magnetization $\theta_M^{opt}(H_0)$ that corresponds to the theoretical dependence $\theta_H^{opt}(H_0)$ (white line), while dashed line indicates the geometrical optimal angle $\theta_M = 35.3^\circ$. The maximum of the LF peak occurs for the particular field $H_0 = 10.7$ Oe, when θ_M in the FMR equals to the ‘geometrical’ optimum 35.3° , which is achieved at $\theta_H = 43.8^\circ$. The similar argumentation can be applied for the HF region as well.

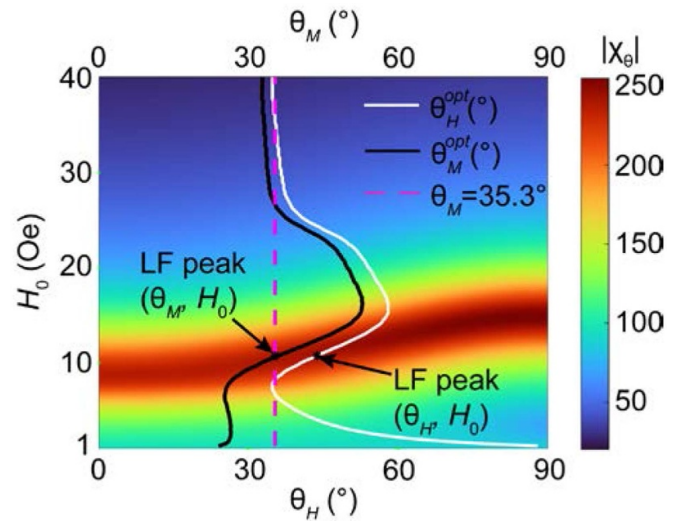


Figure 10. The map showing the susceptibility tensor component $|\chi_\theta|$ as a function of the static field direction θ_H and strength H_0 . On top of the map: the black line shows the calculated optimal angle of the equilibrium magnetization $\theta_M^{opt}(H_0)$ that corresponds to the theoretical dependence $\theta_H^{opt}(H_0)$ (white line), and dashed line indicates the geometrical optimal angle $\theta_M = 35.3^\circ$.

5. Summary and conclusions

In summary, the second harmonic generation in a thin magnetic film has been examined experimentally and theoretically. The studies were carried out on a sample of a thin $\text{Ni}_{80}\text{Fe}_{20}$ film for the relatively low powers (0.02–108 mW) of the input signal at 1 GHz. Studies have shown that the magnetic permeability of the film at a frequency of 1 GHz was high enough to ensure efficient generation of the second harmonic. At the same time, it was also demonstrated that the uniaxial magnetic anisotropy and the field dependence of the damping parameter played a significant role in the generation process. At relatively low frequencies, the magnetic anisotropy field becomes comparable to the FMR field and cannot be neglected when analyzing the second harmonic generation, as is usually done for signals of higher frequencies [21, 23]. In addition, at these low frequencies, it becomes critical to consider the nonlinear dependence of the magnetic damping parameter on the applied field, which is caused by magnetic inhomogeneities in the film.

The detailed measurements for various strength and directions of the applied magnetic field revealed two peaks of second harmonic generation, in the low field (9.5 Oe) and the high one (45.5 Oe). To explain these findings, we have considered a macrospin model of a thin magnetic film with in-plane uniaxial magnetic anisotropy. The Landau–Lifshitz–Gilbert equation was analytically solved for this model in the frame of a perturbation approach, where the dynamic magnetization was expanded in first- and second-order terms. The analysis of the solution showed that the longitudinal component of the second-order magnetization is responsible for the LF peak, which field position coincided with the field of FMR. The HF peak is due to the transverse component of the second-order magnetization that can be excited only by

an ‘oblique’ microwave field. The theoretical analysis also demonstrated that the optimal direction of the applied field, at which the second harmonic generation was maximum, was depended on both the measurement geometry and the FMR conditions.

Considering the measured field dependence of the magnetic damping parameter, uniaxial anisotropy, and both components of the second-order magnetization we have obtained an excellent agreement between the theoretical and experimental results. Understanding the optimal conditions for maximum efficiency of second harmonic generation is pivotal for developing frequency multiplying devices. Such devices, based on ferrites, demonstrated competitive conversion factor at high input powers [15, 17], although in the case of thin metallic magnetic films in coplanar or microstrip waveguides conversion factor was actually quite low [21, 23]. However, it can be significantly increased if instead of the waveguide the microstrip resonator will be used [34]. As a final note, from the analysis of the second harmonic generation power dependence, we have suggested that there were spin wave instability processes for the LF peak but not for the HF one, which is possibly related to the conditions of spin waves excitation. This effect was discussed some time ago for ferrites [20, 35], but there are no such studies for thin metallic magnetic films, which makes it an interesting problem to be addressed in future research.

Data availability statement

The data that support the findings of this study are available upon reasonable request from the authors.

Acknowledgments

This work was supported by the Russian Science Foundation under Grant No. 19-72-10047. The equipment of the Krasnoyarsk Regional Center of Research Equipment of Federal Research Center ‘Krasnoyarsk Science Center SB RAS’ was used during the measurement.

Appendix. Expressions for the dynamic magnetization components

Solution to the zero-order approximation

Solving equation (7), in the notation of figure 1 we obtain

$$H_0 \sin(\theta_H - \theta_M) + \frac{1}{2} H_k \sin 2(\theta_k - \theta_M) = 0. \quad (A1)$$

Numerical calculation of equation (A1) makes it possible to find the angle θ_M of the orientation of equilibrium magnetization \mathbf{M}_0 .

Solution to the first-order approximation

We assume that the linearly polarized microwave driving field is a harmonic signal $\mathbf{h}(t) = \dot{\mathbf{h}} \cdot e^{i\omega_1 t}$ and, therefore, $\mathbf{m}_1(t) = \dot{\mathbf{m}}_1 \cdot e^{i\omega_1 t}$. Substituting the variables $\mathbf{h}(t)$ and $\mathbf{m}_1(t)$, and the effective linear excitation vector $\dot{\mathbf{G}} = (1/M_s)[\dot{\mathbf{h}} \times \mathbf{M}_0]$ into equation (8), we obtain the following solution

$$\dot{\mathbf{m}}_1 = \chi^{(1)} \dot{\mathbf{G}}, \quad (A2)$$

where in projections on the axes ($\mathbf{e}_\theta, \mathbf{e}_y, \mathbf{e}_M$) (see figure 2) $\dot{G}_\theta = h_y, \dot{G}_y = -h_\theta, \dot{G}_M = 0$ and a linear magnetic susceptibility tensor

$$\chi^{(\nu)} = \begin{bmatrix} i\chi_a^{(\nu)} & -\chi_\theta^{(\nu)} & \chi_{13}^{(\nu)} \\ \chi_y^{(\nu)} & i\chi_a^{(\nu)} & \chi_{23}^{(\nu)} \\ 0 & 0 & \chi_m^{(\nu)} \end{bmatrix}, \quad (A3)$$

with components

$$\begin{aligned} \chi_a^{(\nu)} &= \omega_\nu \frac{\gamma M_s}{D_\nu}, \quad \chi_\theta^{(\nu)} = \frac{\gamma M_s}{D_\nu} (\Omega_y + i\omega_\nu \alpha), \\ \chi_{13}^{(\nu)} &= i \frac{\Omega_3}{\omega_\nu} \chi_\theta^{(\nu)}, \quad \chi_y^{(\nu)} = \frac{\gamma M_s}{D_\nu} (\Omega_\theta + i\omega_\nu \alpha), \\ \chi_{23}^{(\nu)} &= \frac{\gamma M_s}{D_\nu} \Omega_3, \quad \chi_m^{(\nu)} = -i \frac{\gamma M_s}{\omega_\nu}, \\ D_\nu &= \Omega_\theta \Omega_y - (1 + \alpha^2) \omega_\nu^2 + i\alpha \omega_\nu (\Omega_\theta + \Omega_z). \end{aligned} \quad (A4)$$

In equation (A4) we also introduce the following notation:

$$\begin{aligned} \Omega_\theta &= \gamma (H_{0M} + (N_{11}^{\text{eff}} - N_{33}^{\text{eff}}) M_s), \\ \Omega_y &= \gamma (H_{0M} + (N_{22}^{\text{eff}} - N_{33}^{\text{eff}}) M_s), \\ \Omega_3 &= \gamma M_s N_{13}^{\text{eff}}, \end{aligned} \quad (A5)$$

where H_{0M} is the projection of the \mathbf{H}_0 vector on the \mathbf{e}_M axis. The main linear magnetic response of the film for the case when $h_y = 0$ (as in the experiment) is expressed by the component

$$\dot{m}_{\theta 1} = \chi_\theta^{(1)} h_\theta = \chi_\theta h_\theta. \quad (A6)$$

Solution to the second-order approximation

Because the effective vector of nonlinear excitation \mathbf{F} included in the right-hand side of the second-order equation (9) is nonlinear, for its calculation we need to use only the real values of the dynamic magnetization and microwave field:

$$\begin{aligned} \mathbf{h}(t) &= (\dot{\mathbf{h}} \cdot e^{i\omega_1 t} + \dot{\mathbf{h}}^* \cdot e^{-i\omega_1 t})/2, \\ \mathbf{m}_1(t) &= (\dot{\mathbf{m}}_1 \cdot e^{i\omega_1 t} + \dot{\mathbf{m}}_1^* \cdot e^{-i\omega_1 t})/2, \end{aligned} \quad (A7)$$

where the asterisk denotes complex conjugate. Substituting expressions (A7) into the effective vector of nonlinear excitation $\mathbf{F} = (1/M_s) \{ \mathbf{h} \times \mathbf{m}_1 + \mathbf{m}_1 \times (N^{\text{eff}} \mathbf{m}_1) \}$ and separating only a part $\mathbf{F}^{(2)}(t) = \dot{\mathbf{F}}^{(2)} \cdot e^{i2\omega_1 t}$ that contains the harmonic at a double frequency $\omega_2 = 2\omega_1$, we obtain

$$\begin{aligned} \dot{\mathbf{F}}^{(2)} &= \frac{1}{2M_s} (\dot{\mathbf{h}} \times \dot{\mathbf{m}}_1 + \dot{\mathbf{m}}_1 \times (N^{\text{eff}} \dot{\mathbf{m}}_1)) = \\ &= \frac{1}{2M_s} \begin{pmatrix} (N_{13}^{\text{eff}} \dot{m}_{\theta 1} \dot{m}_{y1} - \dot{m}_{y1} h_M) \cdot \mathbf{e}_{\theta} + \\ (\dot{m}_{\theta 1} h_M - N_{13}^{\text{eff}} \dot{m}_{\theta 1}^2) \cdot \mathbf{e}_y + \\ - \frac{i\omega_1}{\gamma M_s} \cdot (\dot{m}_{y1}^2 + \dot{m}_{\theta 1}^2) \cdot \mathbf{e}_M \end{pmatrix}. \end{aligned} \quad (\text{A8})$$

Seeking the solution of equation (9) in the form $\mathbf{m}_2(t) = \dot{\mathbf{m}}_2 \cdot e^{i2\omega_1 t}$ for the harmonic component $\mathbf{F}^{(2)}(t)$ of the effective vector of nonlinear excitation \mathbf{F} , we get the following expression for the amplitudes of second order magnetization

$$\dot{\mathbf{m}}_2 = \chi^{(2)} \dot{\mathbf{F}}^{(2)}, \quad (\text{A9})$$

which in the coordinates $(\mathbf{e}_{\theta}, \mathbf{e}_y, \mathbf{e}_M)$ have the following form

$$\begin{aligned} \dot{m}_{\theta 2} &= i\gamma \frac{\omega_2}{2D_2} (N_{13}^{\text{eff}} \dot{m}_{\theta 1} \dot{m}_{y1} - \dot{m}_{y1} h_M) - \\ &\quad - \gamma \frac{(\Omega_y + i\omega_2\alpha)}{2D_2} (\dot{m}_{\theta 1} h_M - N_{13}^{\text{eff}} \dot{m}_{\theta 1}^2) + \\ &\quad + \frac{\omega_1}{2D_2} \frac{\Omega_3}{M_s} \cdot (\dot{m}_{y1}^2 + \dot{m}_{\theta 1}^2), \\ \dot{m}_{y2} &= \gamma \frac{(\Omega_{\theta} + i\omega_2\alpha)}{2D_2} (N_{13}^{\text{eff}} \dot{m}_{\theta 1} \dot{m}_{y1} - \dot{m}_{y1} h_M) + \\ &\quad + i\gamma \frac{\omega_2}{2D_2} (\dot{m}_{\theta 1} h_M - N_{13}^{\text{eff}} \dot{m}_{\theta 1}^2) - \\ &\quad - i \frac{\omega_1}{2D_2} \frac{\Omega_3}{M_s} \cdot (\dot{m}_{y1}^2 + \dot{m}_{\theta 1}^2), \\ \dot{m}_{M2} &= - \frac{1}{4M_s} \cdot (\dot{m}_{y1}^2 + \dot{m}_{\theta 1}^2). \end{aligned} \quad (\text{A10})$$

In the case of a sufficiently thin magnetic film, the out-of-plane magnetization component m_{y1} is close to zero. Therefore, the main contributions to the oscillations at double frequency are from the components $m_{\theta 2}$ and m_{M2} , which can be approximately expressed as

$$\dot{m}_{\theta 2} \approx - \frac{C}{D_2} \dot{m}_{\theta 1} h_M, \quad \dot{m}_{M2} \approx - \frac{1}{4M_s} \dot{m}_{\theta 1}^2, \quad (\text{A11})$$

where $C = \gamma(\Omega_y + i\omega_2\alpha)/2$ varies very slowly with H_0 and can be considered as a constant.

ORCID iDs

P N Solovlev  <https://orcid.org/0000-0003-3545-7599>
 B A Belyaev  <https://orcid.org/0000-0003-4427-4188>
 A V Izotov  <https://orcid.org/0000-0003-0728-3296>
 A A Leksikov  <https://orcid.org/0000-0002-6349-9625>

References

- [1] Wigen P E 1994 *Nonlinear Phenomena and Chaos in Magnetic Materials* (Singapore: World Scientific)
- [2] Livesey K 2015 Nonlinear behavior in metallic thin films and nanostructures *Handbook of Surface Science* vol 5 (Amsterdam: Elsevier) pp 169–214
- [3] Pan R-P, Wei H D and Shen Y R 1989 Optical second-harmonic generation from magnetized surfaces *Phys. Rev. B* **39** 1229–34
- [4] Sampaio L C, Hamrle J, Pavlov V V, Ferré J, Georges P, Brun A, Le Gall H and Ben Youssef J 2005 Magnetization-induced second-harmonic generation of light by exchange-coupled magnetic layers *J. Opt. Soc. Am. B* **22** 119
- [5] Suhl H 1957 The theory of ferromagnetic resonance at high signal powers *J. Phys. Chem. Solids* **1** 209–27
- [6] An S Y, Krivosik P, Kraemer M A, Olson H M, Nazarov A V and Patton C E 2004 High power ferromagnetic resonance and spin wave instability processes in permalloy thin films *J. Appl. Phys.* **96** 1572–80
- [7] Olson H M, Krivosik P, Srinivasan K and Patton C E 2007 Ferromagnetic resonance saturation and second order Suhl spin wave instability processes in thin Permalloy films *J. Appl. Phys.* **102** 023904
- [8] Gui Y S, Wirthmann A and Hu C-M 2009 Foldover ferromagnetic resonance and damping in permalloy microstrips *Phys. Rev. B* **80** 184422
- [9] Zhang X Y and Suhl H 1988 Theory of auto-oscillations in high-power ferromagnetic resonance *Phys. Rev. B* **38** 4893–905
- [10] Kolodin P A, Kabos P, Patton C E, Kalinikos B A, Kovshikov N G and Kostylev M P 1998 Amplification of microwave magnetic envelope solitons in thin yttrium iron garnet films by parallel pumping *Phys. Rev. Lett.* **80** 1976–9
- [11] Khivintsev Y, Kuanr B, Fal T J, Haftel M, Camley R E, Celinski Z and Mills D L 2010 Nonlinear ferromagnetic resonance in permalloy films: a nonmonotonic power-dependent frequency shift *Phys. Rev. B* **81** 054436
- [12] Bragard J, Pleiner H, Suarez O J, Vargas P, Gallas J A C and Laroze D 2011 Chaotic dynamics of a magnetic nanoparticle *Phys. Rev. E* **84** 037202
- [13] Ayres W P, Vartanian P H and Melchor J L 1956 Frequency doubling in ferrites *J. Appl. Phys.* **27** 188–9
- [14] Skomal E N and Medina M A 1958 Microwave frequency conversion studies in magnetized ferrites *J. Appl. Phys.* **29** 423–4
- [15] Risley A S and Kaufman I 1962 Efficient frequency doubling from ferrites at the 100Watt level *J. Appl. Phys.* **33** 1269
- [16] Bady I 1962 Frequency doubling using ferrite slabs, particularly planar ferrites *IEEE Trans. Microw. Theory Tech.* **10** 55–64
- [17] Schied E and Weis O 1984 Microwave-harmonic generation in ferrites at high power *J. Magn. Magn. Mater.* **45** 377–81
- [18] Melchor J L, Ayres W P and Vartanian P H 1957 Microwave frequency doubling from 9 to 18 KMC in ferrites *Proc. IRE* **45** 643–6
- [19] Jepsen R L 1961 Harmonic generation and frequency mixing in ferromagnetic insulators *J. Appl. Phys.* **32** 2627–30
- [20] Al-Bader S J and McStay J 1972 Frequency doubling by oblique pumping of ferrites *Int. J. Electron.* **33** 147–52
- [21] Cheng C and Bailey W E 2013 High-efficiency gigahertz frequency doubling without power threshold in thin-film Ni₈₁Fe₁₉ *Appl. Phys. Lett.* **103** 242402
- [22] Khivintsev Y, Marsh J, Zagorodnii V, Harward I, Lovejoy J, Krivosik P, Camley R E and Celinski Z 2011 Nonlinear amplification and mixing of spin waves in a microstrip geometry with metallic ferromagnets *Appl. Phys. Lett.* **98** 042505
- [23] Marsh J, Zagorodnii V, Celinski Z and Camley R E 2012 Nonlinearly generated harmonic signals in ultra-small waveguides with magnetic films: tunable enhancements of 2nd and 4th harmonics *Appl. Phys. Lett.* **100** 102404
- [24] Bao M, Khitun A, Wu Y, Lee J-Y, Wang K L and Jacob A P 2008 Coplanar waveguide radio frequency ferromagnetic parametric amplifier *Appl. Phys. Lett.* **93** 072509
- [25] Demidov V E, Kostylev M P, Rott K, Krzyszczyk P, Reiss G and Demokritov S O 2011 Generation of the second

- harmonic by spin waves propagating in microscopic stripes *Phys. Rev. B* **83** 054408
- [26] Sebastian T, Brächer T, Pirro P, Serga A A, Hillebrands B, Kubota T, Naganuma H, Oogane M and Ando Y 2013 Nonlinear emission of spin-wave caustics from an edge mode of a microstructured $\text{Co}_2\text{Mn}_{0.6}\text{Fe}_{0.4}$ Si waveguide *Phys. Rev. Lett.* **110** 067201
- [27] Rousseau O, Yamada M, Miura K, Ogawa S and Otani Y 2014 Propagation of nonlinearly generated harmonic spin waves in microscopic stripes *J. Appl. Phys.* **115** 053914
- [28] Gruszecki P, Lyubchanskii I L, Guslienko K Y and Krawczyk M 2021 Local non-linear excitation of sub-100 nm bulk-type spin waves by edge-localized spin waves in magnetic films *Appl. Phys. Lett.* **118** 062408
- [29] Belyaev B A, Izotov A V and Leksikov A A 2005 Magnetic imaging in thin magnetic films by local spectrometer of ferromagnetic resonance *IEEE Sens. J.* **5** 260–7
- [30] Belyaev B A, Boev N M, Gorchakovskiy A A and Galeev R G 2021 Inspection probes of a ferromagnetic resonance scanning spectrometer *Instrum. Exp. Tech.* **64** 277–84
- [31] Belyaev B A, Izotov A V, Solovev P N and Yakovlev I A 2017 Determination of magnetic anisotropies and miscut angles in epitaxial thin films on vicinal (111) substrate by the ferromagnetic resonance *J. Magn. Magn. Mater.* **440** 181–4
- [32] Liu Y, Chen L, Tan C Y, Liu H J and Ong C K 2005 Broadband complex permeability characterization of magnetic thin films using shorted microstrip transmission-line perturbation *Rev. Sci. Instrum.* **76** 063911
- [33] Maksymov I S and Kostylev M 2015 Broadband stripline ferromagnetic resonance spectroscopy of ferromagnetic films, multilayers and nanostructures *Physica E* **69** 253–93
- [34] Belyaev B A, Afonin A O, Ugrymov A V, Govorun I V, Solovev P N and Leksikov A A 2020 Microstrip resonator for nonlinearity investigation of thin magnetic films and magnetic frequency doubler *Rev. Sci. Instrum.* **91** 114705
- [35] Gurevich A G and Melkov G A 1996 *Magnetization Oscillations and Waves* (Boca Raton, FL: CRC Press)
- [36] Schied E 1986 Calculation of nonlinear magnetization components in ferrites *J. Magn. Magn. Mater.* **61** 291–4
- [37] Belyaev B A, Izotov A V, Skomorokhov G V and Solovev P N 2019 Experimental study of the magnetic characteristics of nanocrystalline thin films: the role of edge effects *Mater. Res. Express* **6** 116105
- [38] Schneider M L, Gerrits T, Kos A B and Silva T J 2007 Experimental determination of the inhomogeneous contribution to linewidth in Permalloy films using a time-resolved magneto-optic Kerr effect microprobe *J. Appl. Phys.* **102** 053910
- [39] Harte K J 1968 Theory of magnetization ripple in ferromagnetic films *J. Appl. Phys.* **39** 1503–24
- [40] Craus C B, Chezan A R, Boerma D O and Niesen L 2004 Magnetization dynamics of soft nanocrystalline thin films with random magnetocrystalline anisotropy and induced uniaxial anisotropy *J. Phys.: Condens. Matter* **16** 9227–41
- [41] Hwang T-J, Lee J, Kim K H and Kim D H 2016 Magnetic properties and high frequency characteristics of FeCoN thin films *AIP Adv.* **6** 055914
- [42] Izotov A V, Belyaev B A, Solovev P N and Boev N M 2021 Grain-size dependence of magnetic microstructure and high-frequency susceptibility of nanocrystalline thin films: a micromagnetic simulation study *J. Magn. Magn. Mater.* **529** 167856
- [43] Silva T J, Lee C S, Crawford T M and Rogers C T 1999 Inductive measurement of ultrafast magnetization dynamics in thin-film permalloy *J. Appl. Phys.* **85** 7849–62